Electronic Supplementary Information for:

Measurement of large ribosomal subunit size in cytoplasm and nucleus of living human cells

Aneta Magiera, Karolina Kucharska, Tomasz Kalwarczyk, Patrycja Haniewicz, Karina Kwapiszewska and Robert Hołyst**

This supplement contains the following text, tables, and figures:

S1. Failed targets of YO-PRO-1 dye

We performed *ex vivo*, buffer-based FCS measurements for a number of types of nucleic acids (ssDNA, hairpin, mRNA, tRNA, total pool of RNA), proteins (Human Serum Albumin, HSA), fetal bovine serum (FBS), and HeLa cell lysate. Thus, we proved that the tested dye interacts with tRNA, the total pool of RNA, and cell lysate - both with and without RNAse enzyme (please see section *Research on YO-PRO-1 targets* in the main Manuscript).

As proof that there are no interactions between YO-PRO-1 and ssDNA, hairpin, mRNA, HSA, and FBS, we tracked the fluorescence intensity changes within the time. Such graphs (time traces) for all mentioned potential targets are presented in **Figure S1**.

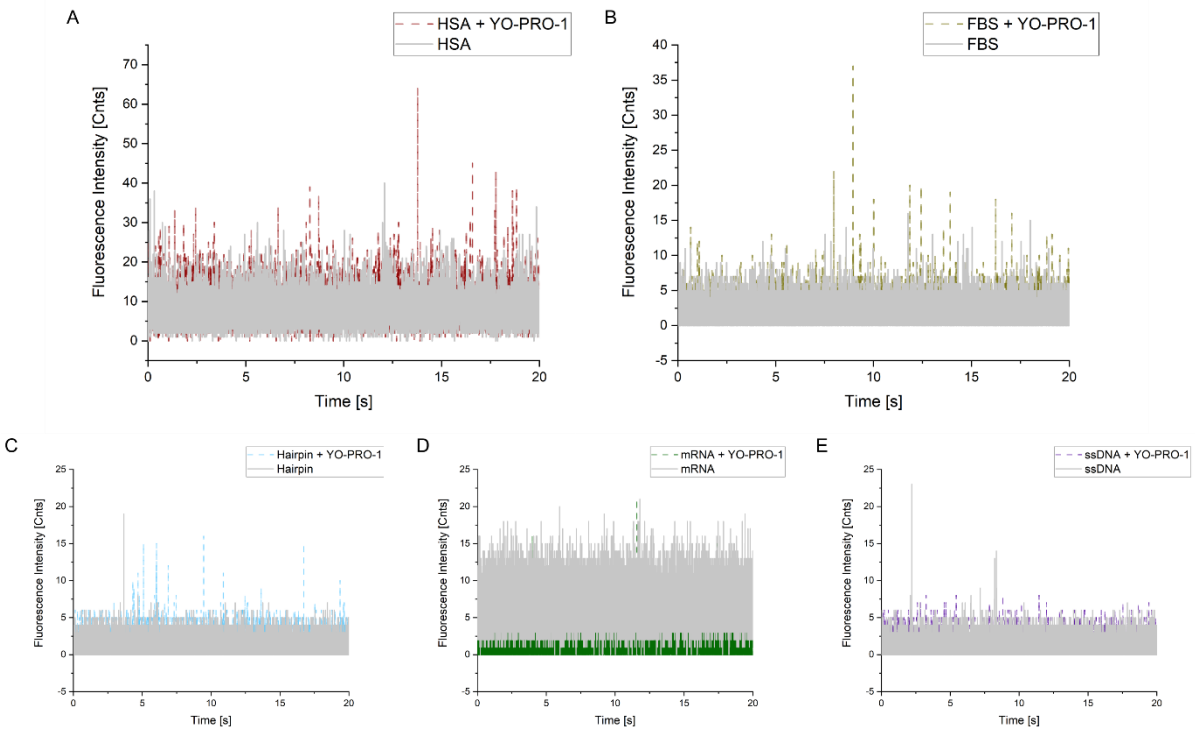

Figure S1. Fluorescence intensity dependence on time for YO-PRO-1 interaction with specific molecules: A) Human Serum Albumin, HSA; B) Fetal Bovine Serum, FBS; C) Hairpin; D) mRNA; E) ssDNA. For all graphs, there is no significant difference between the fluorescence signal from the potential complex with YO-PRO-1 and the tested molecule alone. Thus, we assumed that the dye did not interact with any of the mentioned probes.

S2. The equilibrium constant of YO-PRO-1 with DNA

Analogously to the experiments performed with tRNA, we defined the equilibrium constant between YO-PRO-1 and DNA using the brightness analysis method (BAM). The used double-stranded DNA (69 bp; for DNA sequence, please see Supplementary Information, section S8) was synthesized by ITDNA (United States).

We determined molecular brightnesses γ and α with a ratio of 64. The concentration of binding sites was defined, applying the size of a binding site as 5 base pairs for a single YO-PRO-1 molecule.[1] The averaged equilibrium constant equals to $7.48 \pm 1.95 \cdot 10^5\,M^{-1}$. The value is in good agreement with the literature ($5.78 \pm 0.80 \cdot 10^5\,M^{-1}$).[2] The exemplary curve for DNA fitted with the brightness model and the YO-PRO-1 equilibrium constant determination is shown in **Figure S2**.

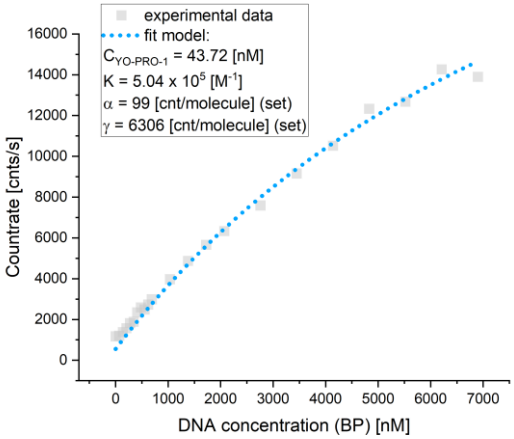

Figure S2. Equilibrium constant determination of YO-PRO-1-DNA (69 bp) complex formation. The dotted line corresponds to the fit of Equation (6). $C_{YO\text{-}PRO\text{-}1}$ is a fitted value of initial dye concentration, K - the equilibrium constant, α is the molecular brightness for a free dye, and γ is the molecular brightness of the formed complex.

S3. Colocalization examination

Two strategies of colocalization analysis were used to identify whether YO-PRO-1, DAPI, and Propidium Iodide stain the same structures in cells. First, a qualitative assessment was performed using Imaris software. Two-channel images were processed with the Colocalization Module, and a colocalization channel was created based on manual thresholding. This strategy aimed at the identification of regions of the cells where both of the analyzed dyes accumulated (see Figure 2F in the main Manuscript).

The second strategy, quantitative, was performed using the JACoP plugin to ImageJ software. The procedure is schematically presented in **Figure S3**. First, two separate channels of the image were extracted. Next, regions of interest (ROIs) were defined in cytoplasmic and nucleus areas separately. Next, one-to-one pixel matching was performed, and Pearson's correlation coefficient was calculated for the data. Pearson's coefficient can be in the range $< -1, 1 >$, where $p = 1$ means perfect correlation, $p = -1$ – anti-correlation, and $p = 0$ indicates no correlation. Results were set in **Table S1**.

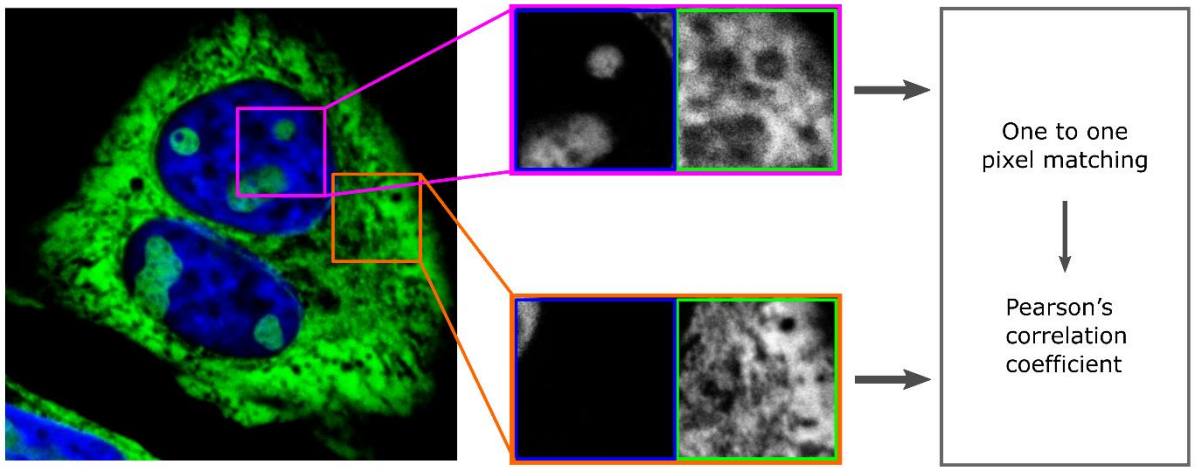

Figure S3. Strategy of quantitative colocalization analysis of confocal images.

Table S1. Pearson's correlation coefficients of the colocalized pixels of pairs of nucleic acids intercalators.

Set of dyes	Correlation coefficient	
	Cytoplasm	Nucleus
YO-PRO-1/DAPI	- 0.290	- 0.315
YO-PRO-1/Propidium Iodide	0.534	0.574
DAPI/Propidium Iodide	0.397	0.221

S4. Length-scale dependent viscosity model in cells

The length-scale dependent viscosity model originated from the detailed studies of polymer solutions. It was observed that viscosity sensed by a probe diffusing in a complex liquid changes with the probes' size: nanobjects experience the viscosity of a solvent, while bigger objects sense macroviscosity. In our previous research,[3,4] we developed a model of length-scale dependent viscosity (LSDV) applicable to complex fluids:

$$\eta_{eff} = \eta_0 A exp\left[b\left(\frac{\xi^2}{{R_H}^2} + \frac{\xi^2}{d^2{r_p}^2}\right)^{\frac{-a}{2}}\right] \quad \text{(S1)}$$

where η_0 is the viscosity of a reference buffer, A is a pre-exponential factor of the order of 1, ξ and R_H are length scales characteristic for a given system, *a* is an exponent of the order of unity, *b* is a parameter dependent on a Debye's screening length, and *d* refers to the probe's caging in complex fluid ($d = 1 + 1.549 * (R_H/\xi)$). In such a fluid, small molecules ($r_p << \xi$), experience viscosity of the solvent, while big tracers ($r_p >> R_H$) experience viscosity measurable by macroscopic methods. Measurements leading to the determination of the model parameters in the cellular interior were reported previously.[3,5] Parameters *b* and *d* are dependent on the geometry of the solution and can be applicable to those fluids, where the geometry of probes and crowders can be, in principle, defined. It was possible in the cell nucleus, where interchromatin channels are filled with proteins. In the case of cytoplasm, the nanostructure and its dynamics are much more complicated, thus, parameters b and d were omitted, and "ξ" refers to an effective parameter. Parameters of the model determined in the nucleus and cytoplasm of HeLa and MDA-MB-231 cells are presented in **Table S2**, and plots of the models are presented in **Figure S4**.

Table S2. Length scale dependent viscosity model parameters derived in HeLa cells.

Compartment	A -	ξ [nm]	R_H [nm]	a -	b -	d -	Reference
Cytoplasm HeLa	1.3 ± 0.3	3.16 ± 0.14	12.9 ± 2.3	0.62 ± 0.07	-	-	[5]
Cytoplasm MDA	1.3 ± 0.3	1.7 ± 0.29	2.85 ± 0.92	0.55 ± 0.15	-	-	[6]
Nucleus	1.4 ± 0.5	24 ± 5.5	3.2	1.29	18.8	1.207	[3]

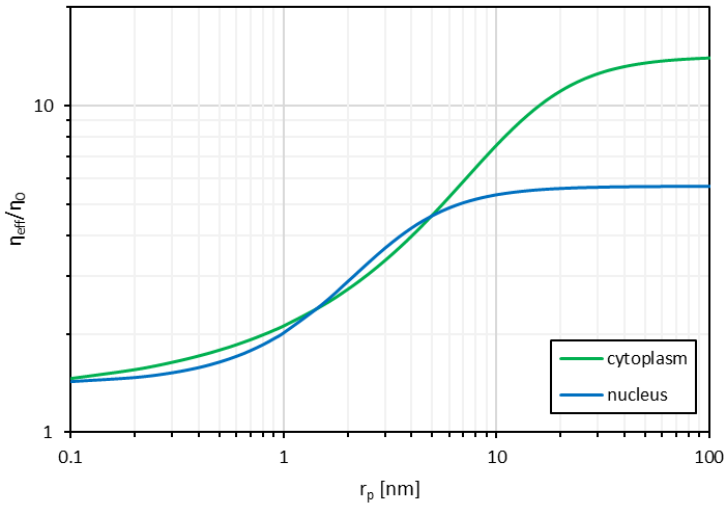

Figure S4. Length scale-dependent viscosity curves in the cytoplasm and nucleus of HeLa cells.

S5. Rotational and translational diffusion fitting model

FCS data from YO-PRO-1 stained cells was fitted with the model describing free, three-dimensional diffusion of two components, one of which exhibits detectable rotations. The core of the model of translational and rotational diffusion was derived from [7] and is presented in Equation (S2-5):

$$G(t) = G_R(t) \times G_T(t) \quad \text{(S2)}$$

$$G_T(t) = \left[\frac{1}{N} \times \left(1 + \frac{t}{\tau_{D_T}}\right)^{-1} \times \left(1 + \frac{t}{\kappa^2 \tau_{D_T}}\right)^{-1/2}\right] \quad \text{(S3)}$$

$$G_R(t) = [1 + A_2 e^{-6D_R t} + A_4 e^{-20D_R t}] \quad \text{(S4)}$$

$$G(t) = [1 + A_2 e^{-6D_R t} + A_4 e^{-20D_R t}] \times \left[\frac{1}{N} \times \left(1 + \frac{t}{\tau_{D_T}}\right)^{-1} \times \left(1 + \frac{t}{\kappa^2 \tau_{D_T}}\right)^{-1/2}\right] \quad \text{(S5)}$$

Where $G_T(t)$ (Equation S3) is a term describing translational diffusion,[8] while $G_R(t)$ (Equation S4) describes rotations. The FCS autocorrelation function is a product of these two terms (Equation S2). Resulting Equation (S5) contains the following parameters: A_2, A_4 – amplitudes of the subsequent rotational terms, D_R – rotational diffusion coefficient (defined by Equation (S6)), N – average number of detectable particles in the focal volume, κ – aspect ratio of the focal volume, τ_{DT} – translational diffusion time of the probe. Parameters D_R and τ_{DT} are not independent, as they both depend on the hydrodynamic radius of a probe, r_p, as presented in Equations (S6-9):

$$D_R = \frac{k_B T}{8\pi\eta_R {r_p}^3} \quad \text{(S6)}$$

$$\tau_{D_T} = \frac{{\omega_0}^2}{4D_T} \quad \text{(S7)}$$

$$D_T = \frac{k_B T}{6\pi\eta_T r_p} \quad \text{(S8)}$$

$$\tau_{D_T} = \frac{3{\omega_0}^2 \pi\eta_T r_p}{2k_B T} \quad \text{(S9)}$$

Where k_B is Boltzmann constant, T is temperature in Kelvin, η_R, η_T are effective viscosities sensed at the level of rotation and translation, respectively (as explained in [9]), and ω_0 is a shorter radius of a focal volume. Substitution of Equations (S6) and (S9) into Equation (S5), resulted in Equation (S10), where r_p is a fitting parameter:

$$G(\tau) = \left\{1 + \left[fA_2 exp\left(-\frac{6\tau k_B T}{8\pi\eta_R {r_p}^3}\right)\right] + \left[fA_4 exp\left(-\frac{20\tau k_B T}{8\pi\eta_R {r_p}^3}\right)\right]\right\} \times \left\{\frac{1}{N} \times \left[1 + \frac{2\tau k_B T}{3\pi\eta_T \omega_0^2 r_p}\right]^{-1} \times \left[1 + \frac{2\tau k_B T}{3\pi\eta_T \omega_0^2 \kappa^2 r_p}\right]^{-1/2}\right\} \quad \text{(S10)}$$

Equation (S10) describes the rotational and translational diffusion of a single fluorescent component in a sample. However, Equation (S10) did not fit the experimental data, as presented in **Figure S5**. One component model clearly did not describe the motion of the fluorescent components of the sample.

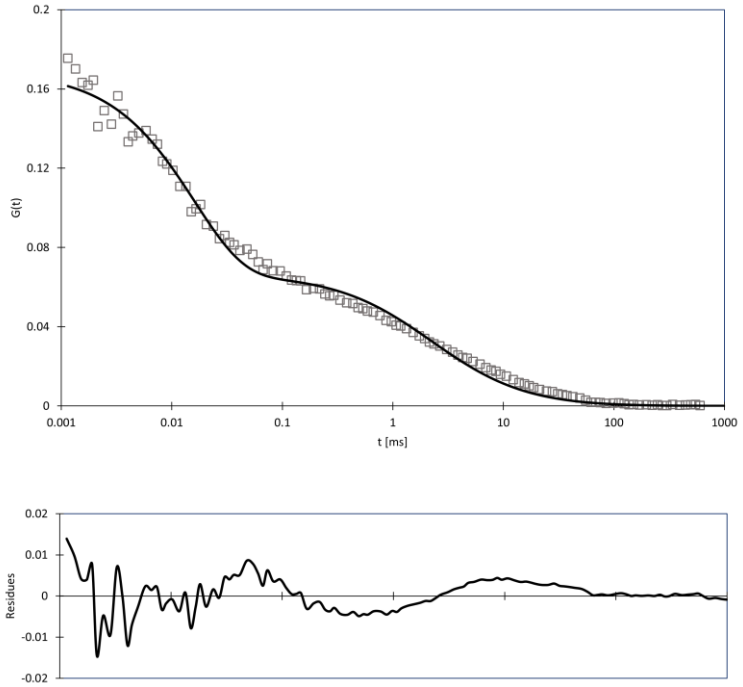

Figure S5. FCS data of YO-PRO-1 stained cytoplasm fitted with Equation (S10). Significant discrepancies between data and the model were observed.

Based on *ex vivo* experiments, we identified DNA, tRNA, and rRNA as the most probable acceptors of YO-PRO-1. DNA was excluded from possible FCS curve contribution due to its immobility in the time scales of the experiment. Among the remaining RNA-based particles, we discussed their probability of YO-PRO-1 binding in the S6 section. Based on our estimations, the order of YO-PRO-1 mobile acceptors is: (I) 60S ribosomal large subunits (LSU), (II) tRNA (all types), and (III) 40S ribosomal small subunits (SSU). We assumed that the major component is the 60S subunit. Thus, the first extension of the model was the addition of a term describing the diffusion of tRNA. *Ex vivo* experiments revealed r_{tRNA} = 2 nm, thus, characteristic times of rotations of tRNA are at the order of 10 ns, which is beyond the detectable timescales of our FCS setup and, therefore, could have been neglected in the formula.

Consequently, only the translational diffusion term, with the analogy to Equation (S3), was added to Equation (S10), resulting in Equation (S11):

$$G(\tau) = \left[\mathrm{q}\left(\left\{1 + \left[fA_2 exp\left(-\frac{6\tau k_B T}{8\pi\eta_R {r_{LSU}}^3}\right)\right] + \left[fA_4 exp\left(-\frac{20\tau k_B T}{8\pi\eta_R {r_{LSU}}^3}\right)\right]\right\} \times \left\{\frac{1}{N} \times \left[1 + \frac{2\tau k_B T}{3\pi\eta_T \omega_0^2 r_{LSU}}\right]^{-1} \times \left[1 + \frac{2\tau k_B T}{3\pi\eta_T \omega_0^2 \kappa^2 r_{LSU}}\right]^{-1/2}\right\}\right) + (1-q)\left(\left\{\frac{1}{N} \times \left[1 + \frac{2\tau k_B T}{3\pi\eta_{T,tRNA} \omega_0^2 r_{tRNA}}\right]^{-1} \times \left[1 + \frac{2\tau k_B T}{3\pi\eta_{T,tRNA} \omega_0^2 \kappa^2 r_{tRNA}}\right]^{-1/2}\right\}\right)\right] \quad \text{(S11)}$$

Details of the parameters of Equation (S11) are listed in **Table S3**. We reduced fitting parameters only to amplitudes (ratios between components) and hydrodynamic radius of a large ribosomal subunit. The rest of the parameters were fixed based on control experiments and theoretical models.

Table S3. Parameters of the fitting model (Equation (S11)).

Parameter	Value	Fixed	Details
q	fitted	-	Relative fraction of 60S sunbunits to tRNA molecules, fitted in the range <0,1>
f	fitted	-	Amplitude of rotational diffusion
A_2	1,1071	✓	Amplitude of a rotational term, fixed for the value calculated based on [7]
A_4	0,0464	✓	Amplitude of a rotational term, fixed for the value calculated based on [7]
k_B	$1.38 \cdot 10^{-23}$ J/K	✓	Boltzmann constant
T	309.14 K	✓	Temperature set for the experiment
r_{LSU}	fitted	-	Radius of a ribosomal 60S subunit
η_R	varied	✓	Effective viscosity for rotational diffusion of ribosomal 60S subunit, based on the models presented in [3,5], calculated with the respect to work of [9]. Fixed and changed iteratively to match fitted r_{LSU}
η_T	varied	✓	Effective viscosity for translational diffusion of ribosomal 60S subunit, based on the models presented in [3,5]. Fixed and changed iteratively to match fitted r_{LSU}

ω_0	~ 200 nm	✓	Size of the focal volume, determined during calibration preceding each experiment[10]
κ	~ 6	✓	Aspect ratio of the focal volume, determined during calibration preceding each experiment[10]
N	fitted	-	Average number of fluorescent molecules in the focal volume
r_{tRNA}	2 nm	✓	Hydrodynamic radius of tRNA molecules, determined experimentally in a buffer with FCS
$\eta_{T,tRNA}$	• 0.001936 Pa·s in cytoplasm • 0.00205 Pa·s in nucleus	✓	Effective viscosity for translational diffusion of tRNA (r_p=2 nm), based on the models presented in [3,5]

Example fitting of the model with and without tRNA component to the data acquired in cytoplasm and nucleus is presented in **Figure S6**. Significantly better fit was observed after adding the tRNA term. Following this pattern, the next model, with the addition of rotation and translation of 40S small subunits, was added. However, the added terms did not improve fit quality.

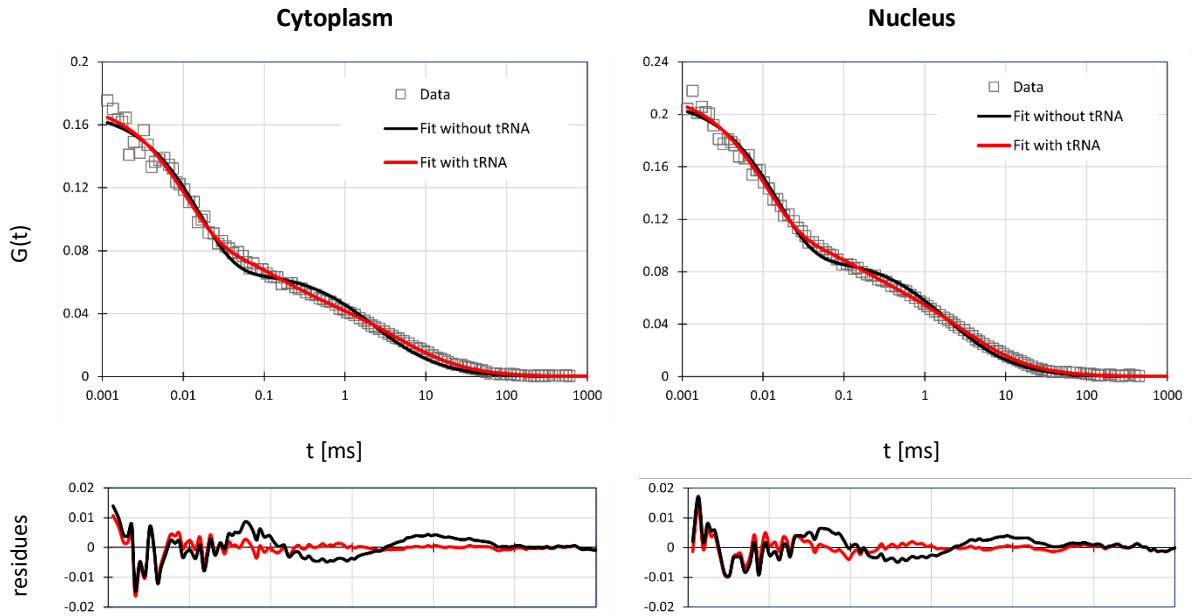

Figure S6. Comparison of fitting Equation (S10) ("Fit without tRNA") and Equation (S11) ("Fit with tRNA") to the FCS data acquired in cytoplasm and nucleus of YO-PRO-1 stained HeLa cells.

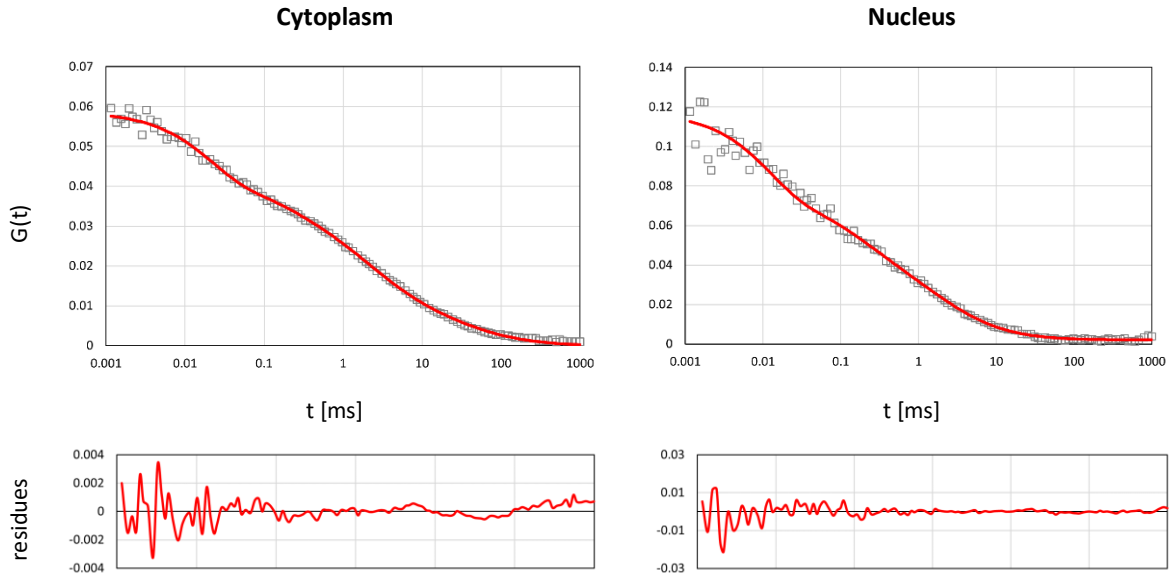

Figure S7. Example fits of the Equation (S11) to FCS curves obtained in MDA-MB-231 cells stained with YO-PRO-1. In the case of the nucleus, the hydrodynamic radius of LSU was fixed, and only amplitudes of components were fitted – perfect fit was achieved.

Table S4. Results of FCS data fitting in YO-PRO-1 stained cells.

		Hydrodynamic radius of LSU r_{LSU} [nm]	Fraction of LSU in FCS q [%]	Effective viscosity for rotations η_R [mPa·s]	Effective viscosity for translation η_T [mPa·s]
HeLa	Cytoplasm	14.6 ± 1.7	52 ± 5	3.69 ± 0.48	9.76 ± 1.37
	Nucleus	14.8 ± 0.9	75 ± 11	3.68 ± 0.04	3.88 ± 0.01
MDA-MB-231	Cytoplasm	17.1 ± 1.96	52 ± 14	3.36 ± 0.03	3.43 ± 0.01
	Nucleus	14.8*	64 ± 14	3.68*	3.88*

* values fixed based on HeLa results, curves fitted well with only amplitudes fitted

Table S5. Diffusion coefficients of LSU and tRNA in the cellular interior.

		LSU		tRNA	
		D_{rot} [μs^{-1}]	D_{trans} [$\mu m^2/s$]	D_{rot} [μs^{-1}]	D_{trans} [$\mu m^2/s$]
HeLa	Cytoplasm	0.011	2.2	16	58.5
	Nucleus	0.014	3.9	17	55.2
MDA-MB-231	Cytoplasm	0.015	4.4	12	46.4

	Nucleus	0.014	3.9	17	55.2

S6. Possibility of YO-PRO-1 staining of intracellular RNA molecules

To estimate the probability of observation of certain RNA molecules stained with YO-PRO-1 in the FCS signal, the following factors were considered:

(1) Estimation of size/mobility of RNA molecules
(2) Estimation of the brightness of individual RNA molecules
(3) Estimation of abundance/accessibility of RNA molecules for staining

1. Size of RNA molecules.

FCS is a technique that detects the motion of fluorescent particles. Thus, immobile molecules cannot be analyzed by FCS. Among possible YO-PRO-1 targets, we consider tRNA, 40S rRNA, 60S rRNA, and 80S ribosomes. 80S ribosomes are not freely diffusing particles, as they are assembled on mRNA molecules and form translation complexes.[11] The diffusion coefficient of the translation complex is ~0.05 $\mu m^2/s$ in HeLa cells, according to [12], and it corresponds to objects as big as ~500 nm (following length scale-dependent viscosity model[5]). Such big objects do not exhibit free diffusion in the cytoplasm,[12] as they are bigger than average pore size (~100 nm) in a gel-like structure of the cell.[4] Moreover, following Equation (S7), the expected diffusion time of objects of D = 0.05 $\mu m^2/s$ would be equal to ~250 ms, while no autocorrelation was observed in such a timescale (see Figure S6). Thus, 80S ribosomes were excluded from the pool of possible FCS curve components. We assumed that the rest of the RNA molecules (40S, 60S and tRNA), can contribute to the FCS signal.

2. Estimation of the brightness of YO-PRO-1 stained RNA molecules.

The average number of freely diffusing molecules detected in YO-PRO-1 stained HeLa cells was ~15/focal volume, which corresponds to a concentration of ~40 nM. The number of ribosomes in HeLa cells is around $3 \cdot 10^6$/cell,[13] out of which ~15% can be considered as free subunits (in fast-dividing cells[14]). This gives ~400 nM concentration of each of the free subunits. Additionally, there are ~10 tRNA molecules per 1 ribosome in an eucaryotic cell,[15] which gives a concentration of ~27 μM. Thus, there is a ~500-fold extend of RNA molecules to YO-PRO-1 stained molecules. Therefore, in our experimental conditions, on average, each visible RNA molecule is bound to one YO-PRO-1 molecule, and each molecule contributing to the FCS signal should exhibit the same brightness.

However, time of rotation can additionally influence the apparent brightness of a molecule. The fluorophore can absorb the photon only when its spatial orientation is in a certain position with respect to the polarized laser beam.[7] Thus, the probability of fluorescence detection from a single fluorophore-labeled molecule is inversely proportional to its rotation time – molecules rotating faster would be

apparently brighter. We considered this effect and provided rotation time estimations in **Table S6**. The frequency of rotations of tRNA molecules is 3 orders of magnitude higher than that of ribosomal subunits. Thus, there is a considerably higher probability of observing photons originating from a single-stained tRNA molecule than a rRNA molecule.

Table S6. Estimation of the number of rotations of rRNA and tRNA molecules.

Probe	r_p [nm]	Cytoplasm		Nucleus	
		τ_{rot} [µs]†	rotations per second	τ_{rot} [µs]‡	rotations per second
LSU	14.6 *	22.4	$4.5 \cdot 10^4$	12	$8.3 \cdot 10^4$
SSU	12 **	10.2	$9.8 \cdot 10^4$	6	$1.7 \cdot 10^5$
tRNA	2 *	0.015	$6.7 \cdot 10^7$	0.01	$1 \cdot 10^8$

* measured by FCS

** estimated based on molecular mass of SSU in comparison to LSU

† Calculated using formulas derived from cytoplasm in [5,9]

‡ Calculated using formulas derived for the nucleus in [3,9]

3. Estimation of accessibility of RNA molecules for staining.

YO-PRO-1 is a double-strand nucleic acid intercalator.[1,2] We analyzed secondary structures of tRNA, SSU RNA, and LSU RNA to estimate the number of possible YO-PRO-1 binding sites per molecule. Secondary structures of RNA were obtained from https://rnacentral.org/, and the following entries were analyzed:

- LSU: 28S rRNA (URS0000ABD8B3_9606), 5.8S rRNA (URS0000005270_9606), 5S rRNA (URS00000F9D45_9606)
- SSU: 18S rRNA (URS0000704D22_9606)
- tRNA: t-RNA-Met (URS0000145C5E_9606)

A number of base pairs involved in double-strand sequences are summarized in histograms in **Figure S8**. Briefly, LSU contains 1516 base pairs, SSU – 472 bp, and tRNA – 21 bp.

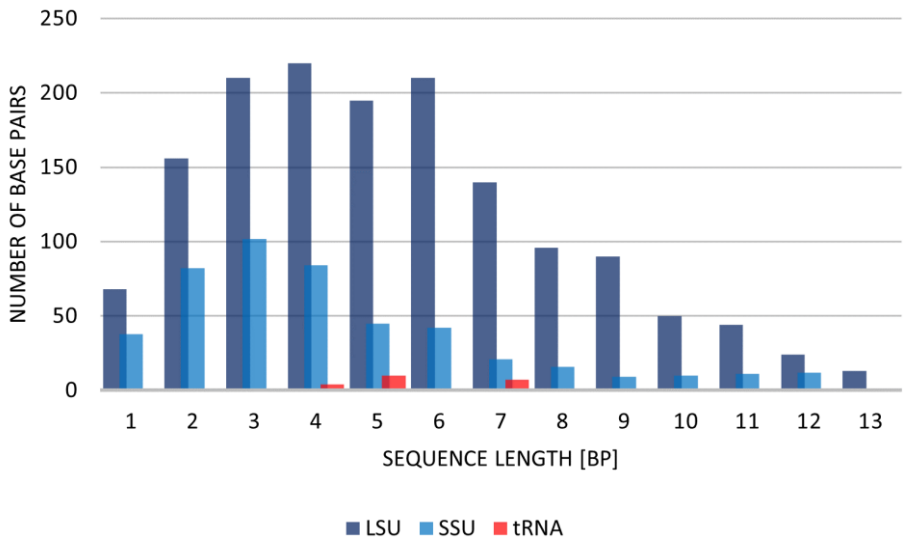

Figure S8. Number of base pairs in given sequence length in the secondary structures of ribosomal subunits and tRNA.

Assuming (a) 10:1 ratio of tRNAs to ribosomes, (b) 1:1 ratio of LSU to SSU, (c) 15% fraction of free subunits, and (d) every 5 bp sequence (or longer) as a potential binding target for YO-PRO-1,[1] we calculated abundance of potential binding sites: $6.3 \cdot 10^7$ sites/cell on LSU, $1.3 \cdot 10^7$ sites/cell on SSU, and $9 \cdot 10^7$ sites/cell on tRNA. Given numbers would result in relative amplitudes in FCS of 0.38, 0.08, and 0.54, respectively. The actual amplitudes registered in the cytoplasm and nucleus of HeLa cells did not match the theoretical ones – most probably, there is another factor connected with base pairs availability from the outside of a molecule. In **Figure S9**, we simulated how YO-PRO-1 steric restrictions, or altered ratio between ribosomal subunits, would influence FCS amplitudes. According to the simulations, it is most likely that the ratio of the number of freely diffusing LSU to SSU is larger than 1.

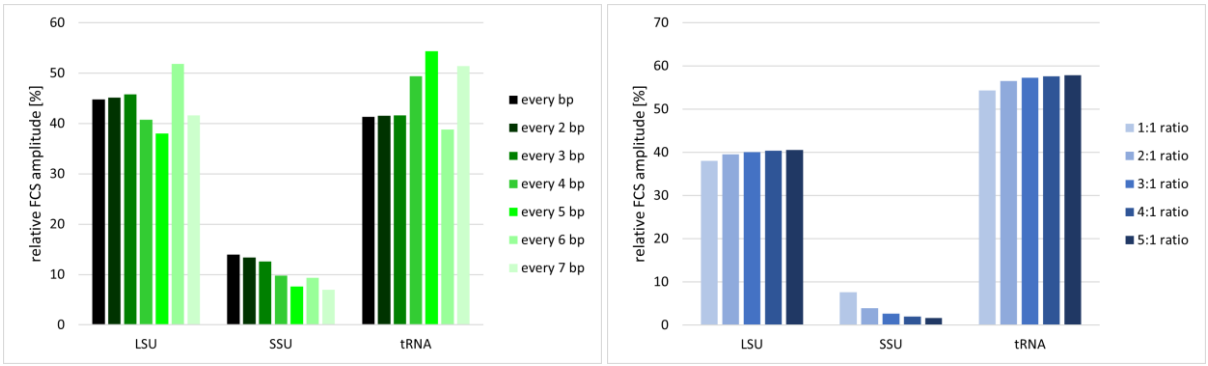

Figure S9. Simulation of expected FCS amplitudes as a result of altered YO-PRO-1 spacing of double-stranded RNA (left) and altered ratio of the number of LSU to SSU (right).

S7. *In silico* determination of ribosomal large subunit hydrodynamic radius

Calculation of hydrodynamic radii using Hydrosub software

We calculated the hydrodynamic radius of the large ribosomal subunit for three structures obtained from the Protein Data Bank and published in reference.[16] The procedure was as follows. First, we imported the given file containing the biological assembly of the ribosomal subunit into the PyMOL [The PyMOL Molecular Graphics System, Version 2.0 Schrödinger, LLC] software. The biological assembly represented as a surface was exported to the .wrl file and further imported to the Blender 3d software [blender.org]. The whole complex was manually oriented in 3D to orient the longest semiaxis along the Z-axis. Next, we removed all the mesh vertices hidden inside the structure. The vertices forming the outer shell were left untouched. We further fitted the shell vertices in the 3D space with the ellipsoid Equation:

$$\frac{x^2}{a^2}+\frac{y^2}{b^2}+\frac{z^2}{c^2}=1 \qquad \text{(S12)}$$

The next two values of the two shortest semiaxes were averaged. The representation of the biological assembly for the 6LU8 structure is shown in the **Figure S10**.

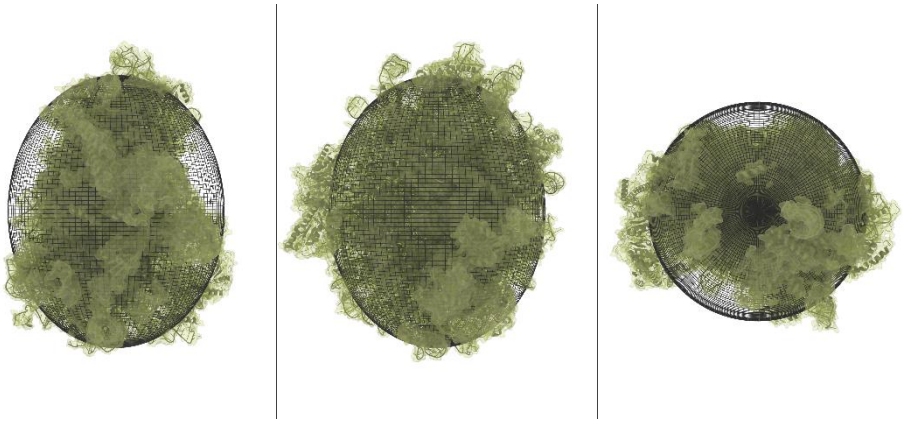

Figure S10. The figure represents a complete biological assembly of the large ribosomal subunit (surface of the subunit and the cartoon representation inside) along with the ellipsoid fitted to the outer shell of the assembly surface). The figure depicts the same subunit observed along X, Y, and Z axis, respectively.

The obtained values of semiaxes were further used as input values in the Hydrosub software,[17] which fits the hydrodynamic properties of protein subunits represented as ellipsoids. In our case, we used only one ellipsoid per structure. Obtained values of the Stokes hydrodynamic radius are shown in **Table S7**.

Table S7. Fitted values of the Stokes hydrodynamic radius obtained by different models.

pdb Id	R_h [nm][a]	R_h [nm][b]	R_h [nm][c]
6LU8	17.5	16	9.7
6LSR	17.4	16	9.9
6LQM	17.2	15.8	9.8

[a] Calculated from molecular weight using Equation (1) from reference [18]

[b] Calculated from molecular weight using Equation (2) from reference [18]

[c] Calculated based on the tertiary structure using Hydrosub software, as explained in the text.

S8. Measurement of ribosomal subunits in a buffer

Hydrodynamic radii of SSU, LSU, and ribosomes isolated by microcentrifugation were measured using FCS. Samples originated from subunit isolation were diluted in B buffer (see Experimental Section), incubated with YO-PRO-1 (~5 nM), and subjected to FCS at 25°C. The system was calibrated using Rho110 in B buffer (see Experimental Section) with a viscosity equal to 1.04 mPa·s (25°C).

FCS curves obtained from SSU (40S) were fitted with the simplest one-component free diffusion model (without rotational term, Equation S3), confirming only one type of fluorescently labeled molecules in the sample. An example FCS curve, with a fitted model and residues, is presented in **Figure S11**.

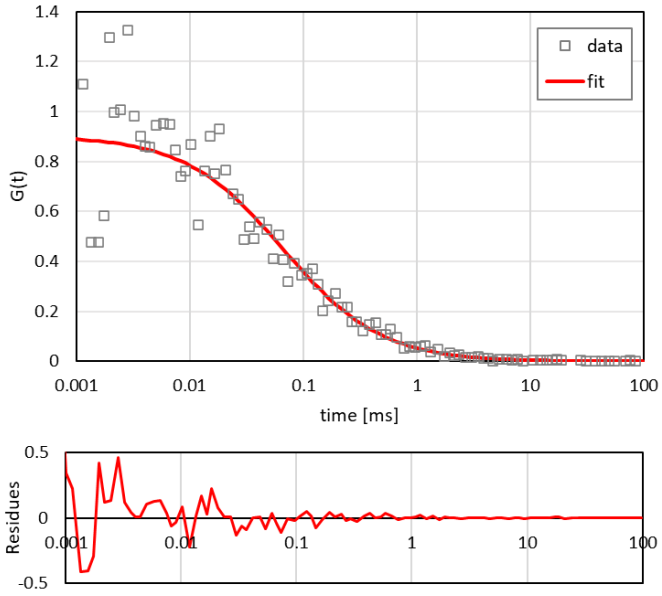

Figure S11. Results of fitting of Equation (S3) to FCS data from YO-PRO-1 stained SSU in B buffer (see Experimental Section).

FCS curves for LSU (60S) in a buffer contained visible rotational diffusion term in the 1-10 µs timescales. Thus, a single component translational and rotational diffusion model (S10) was fitted to the data, with r_p (hydrodynamic radius) as a fitting parameter. An example curve for the fitted model is presented in **Figure S12**.

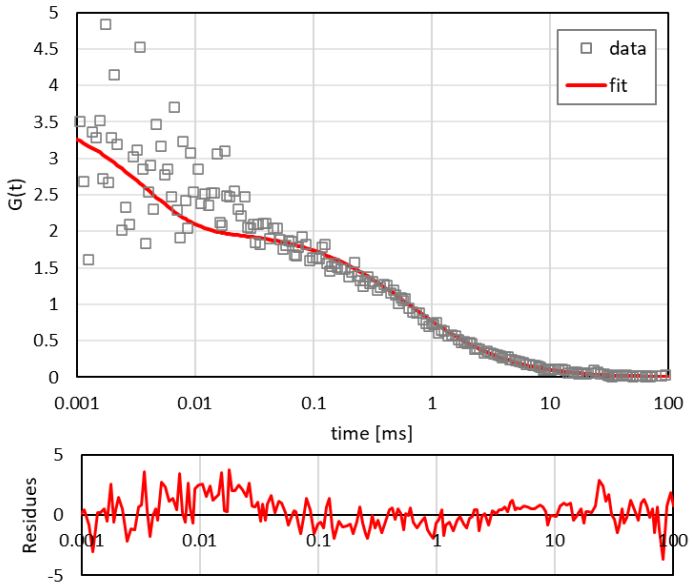

Figure S12. Results of fitting of Equation (S10) to FCS data from YO-PRO-1 stained LSU in B buffer (see Experimental Section).

FCS curves obtained for the 80S sample (whole ribosomes) also contained rotational diffusion term. However, fitting with Equation (S10) was not successful due to the presence of some big, slowly diffusing additional objects (characteristic timescales >10 ms). Thus, curves were fitted with Equation (S11), with τ_{tRNA} replaced with an unknown τ_D, as an additional fitting parameter. Example fit is presented in **Figure S13**. All hydrodynamic radii of ribosomal subunits measured by FCS in the buffer are presented in **Table S8**.

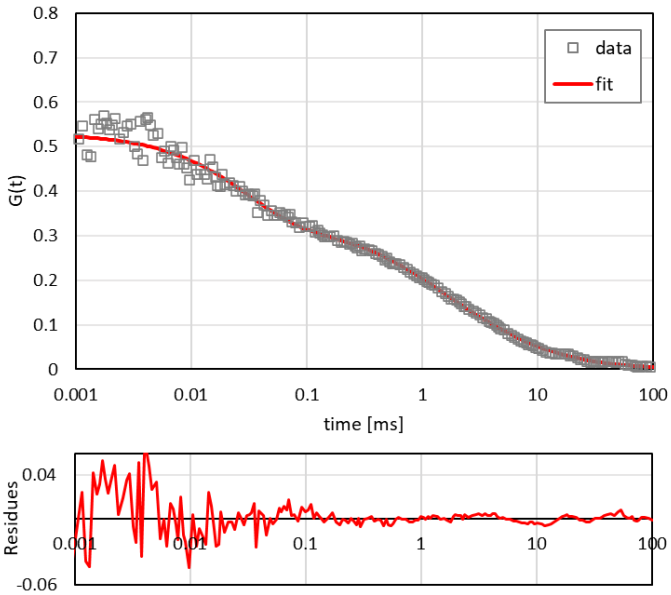

Figure S13. Results of fitting of Eqation (S11) to FCS data from YO-PRO-1 stained 80S ribosomes sample in B buffer (see Experimental Section).

Table S8. Hydrodynamic radii of 80S, 60S, and 40S ribosomal subunits measured in a buffer at 25°C.

Sample	Fitted model	Hydrodynamic radius r_p [nm]
40S ribosome (SSU)	Equation (S3)	3.8 ± 0.8
60S ribosome (LSU)	Equation (S10)	15.0 ± 2.7
80S ribosome	Equation (S11)	31.6 ± 1.5

S9. Influence of rapamycin and doxorubicin on LSU abundance and diffusion in living HeLa cells

Cells were subjected to rapamycin (Rap) and doxorubicin (Dox) for 6 hours and then stained with YO-PRO-1 dye to visualize ribosomes and tRNA. FCS curves were collected in both the cytoplasm and nucleus of Rap- and Dox-exposed cells, as well as in the native cells as a control. FCS curves were fitted with the model Equation (S11), with only r_{LSU} and q_{LSU} as fitting parameters. The results of the experiments are presented in Figures S14-S16.

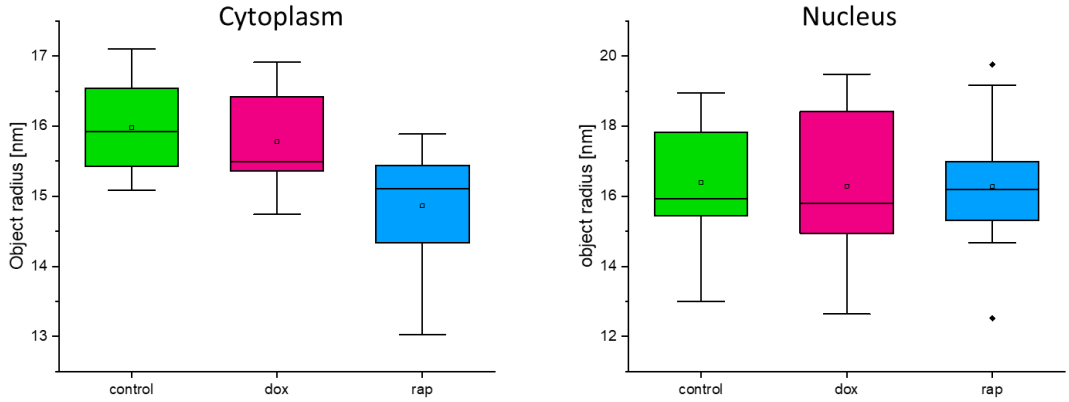

Figure S14. Results of measurements of rLSU in native, dox-, and rap-exposed cells. LSU radius was measured to decrease under rapamycin influence.

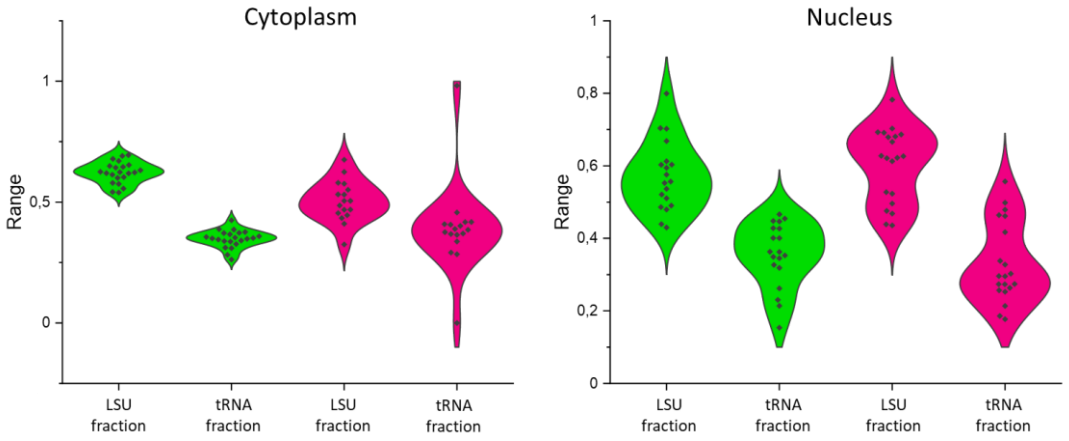

Figure S15. Changes in LSU to tRNA proportion in cells exposed to doxorubicin for 6 hours. No significant changes were detected both in the cytoplasm and nucleus.

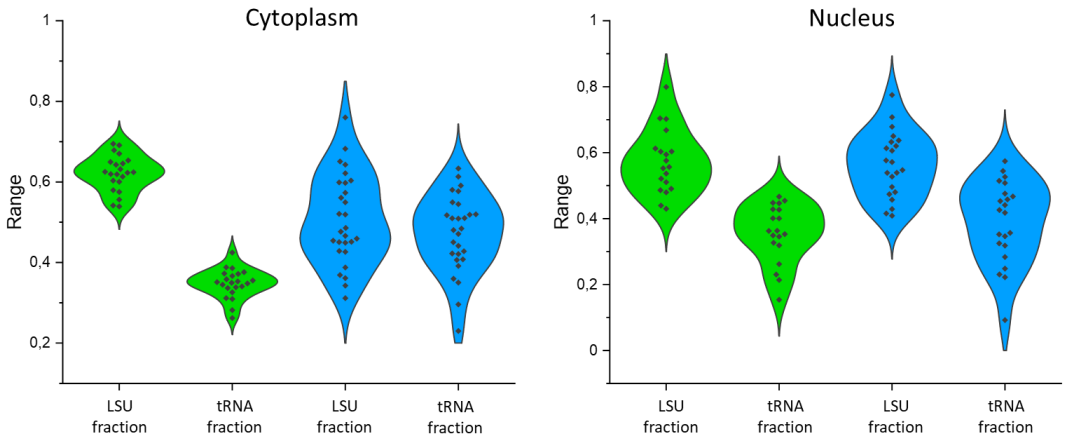

Figure S16. Changes in LSU to tRNA proportion in cells exposed to rapamycin for 6 hours. In the cytoplasm, it was observed that the fraction of LSU decreased. No significant changes were detected in the nucleus.

The LSU to tRNA amplitudes ratio was calculated for control and rap-exposed cells. Then, statistical analysis was performed using the Analysis ToolPak add-in to Microsoft Excel Software. The datasets were compared using a two-sample t-test assuming unequal variances. The difference between samples was significant, with $p<0.0005$.

S10. DNA sequence

In the brightness experiments, we used a 69 bp double-stranded oligonucleotide synthesized by Integrated DNA Technologies, Iowa, US.

5’	GAT	ACG	AGC	ATC	GTG	TAG	GCA	TCG	TAG	GTA	ATA	(…)
3’	CTA	TGC	TCG	TAG	CAC	ATC	CGT	AGC	ATC	CAT	TAT	(…)
(…)	CGG	ATG	TGC	TAG	CTT	ATT	GAA	TTC	AGA	GAT	CTA	TGC 3’
(…)	GCC	TAC	ACG	ATC	GAA	TAA	CTT	AAG	GAG	CTA	GAT	ACG 5’

S11. Parameters determination of brightness analysis method

To properly calculate equilibrium constants for YO-PRO-1 reactions with DNA and tRNA, we calculated additional parameters:

(1) Determination of the effective focal volume
(2) Determination of appropriate laser power
(3) Determination of molecular brightnesses of the YO-PRO-1 dye and formed complexes with DNA and tRNA

1. Determination of focal volume

We calibrated the FCS set-up prior to measurements, utilizing fluorescent dye with known size and diffusion coefficient. We used rhodamine 110 (D = 580 $\frac{\mu m^2}{s}$) at temperature applied in measurements (36 °C) to determine semi-minor axis of the confocal volume (ω) and the effective focal volume (V_{eff}). We performed 24 separate measurements of the dye and fitted the data with a one-component diffusion autocorrelation function with a triplet state (Eqn. S13).

$$G_T(t) = \left[\frac{1}{N} \times \left(1 + \frac{T}{1+T} \cdot \left(exp\frac{t}{\tau_{trip}}\right)^{-1}\right) \times \left(1 + \frac{t}{\tau_{D_T}}\right)^{-1} \times \left(1 + \frac{t}{\kappa^2 \tau_{D_T}}\right)^{-1/2}\right] \qquad \text{(S13)}$$

where T is the fraction of the triplet state in the signal and τ_{trip} is a triplet lifetime. The autocorrelation functions were exported and analyzed with a self-written Python script using an appropriate diffusion model based on Equation (S1) with a nonlinear least square fitting method (**Figure S17**).
The obtained values from measurements were averaged, and the semi-minor axis of the confocal volume ω was calculated using the formula:

$$\omega = \sqrt{4\tau D} \qquad \text{(S14)}$$

Then, the determined value of omega was used to calculate the effective focal volume, V_{eff}:

$$V_{eff} = \pi^{3/2} \cdot \kappa \cdot \omega^3 \qquad \text{(S15)}$$

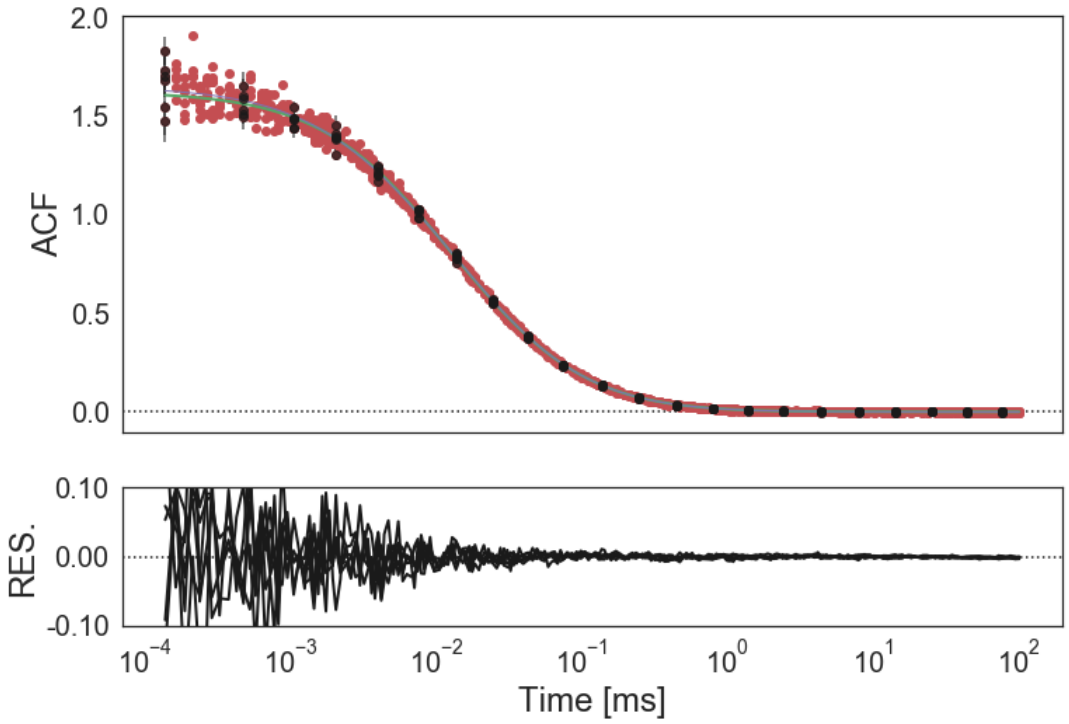

Figure S17. Example of the FCS autocorrelation curves obtained in the calibration. The measuring time for each autocorrelation curve was 20 s. The data were fitted with a one-component diffusion model, including the triplet state contribution (Eqn S13). Red points represent experimental data, and the black line is the autocorrelation fitted function. The bottom panel shows the residual curve (the difference between experimental and fitted data).

2. Determination of appropriate laser power

Free YO-PRO-1 has a low quantum yield. We measured YO-PRO-1 dye in a wide range of laser powers (**Figure S18**) to determine its appropriate value, allowing us to avoid photobleaching of the dye. The increase in laser power does not influence the dye's fluorescence properties. We do not detect autocorrelation function in any of the used laser powers.

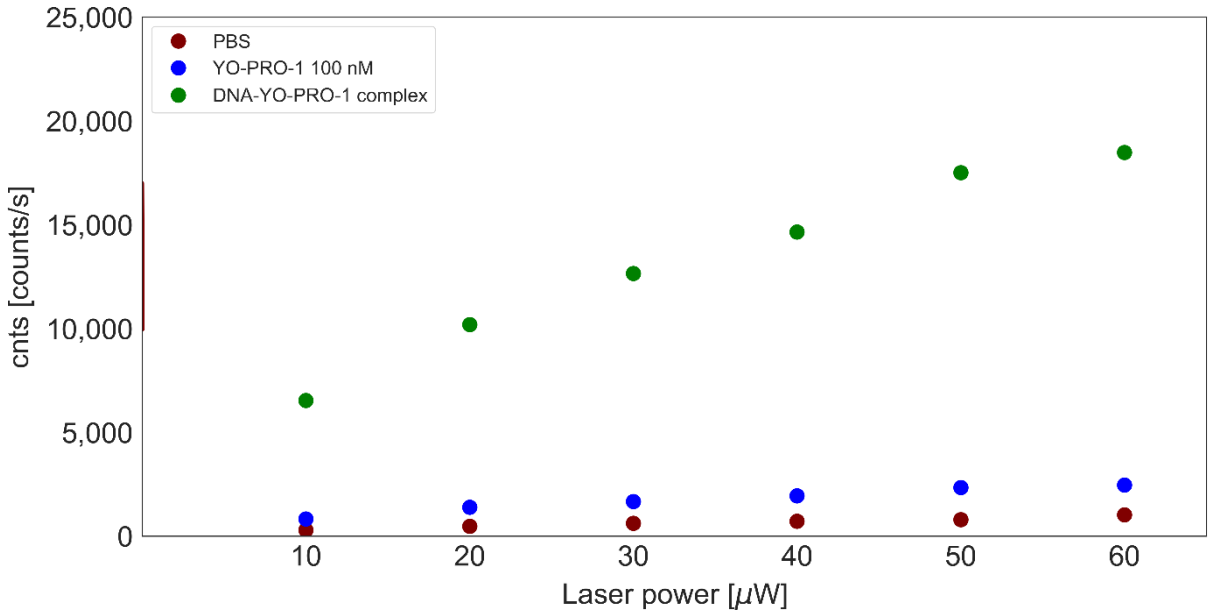

Figure S18. Response of the samples after excitation with different laser power. PBS and YO-PRO-1 dye do not show fluorescence; the collected signal comes from the dispersion of the laser beam on molecules. The complex of DNA (100 nM) and YO-PRO-1 (20 nM) exhibit fluorescence properties. Response from the sample is linear in the laser power below 30 μW. For higher powers, the complex is photo-bleaching during the measurement, and the sample response is not linear.

3. Determination of molecular brightnesses of the YO-PRO-1 dye and formed complexes with DNA and tRNA

We experimentally determined the molecular brightness of the free YO-PRO-1 dye (α) and the formed complexes with DNA (γ_{DNA}) and tRNA (γ_{tRNA}). In a free state, YO-PRO-1 exhibits weak fluorescence properties. The registered signal comes from the dispersion of the laser beam on the dye molecules. We used a 1000 nM dye concentration and performed an FCS measurement. Collected photons were then divided by the statistical number of molecules present in the focal volume.

For determination γ_{DNA}, we measured the sample with excess binding sites using a DNA concentration of 500 nM and a dye of 40 nM. Then, we calculated the number of molecules as an inversion of G_0 (value of the autocorrelation function at a point where experimental data start). We divided the collected number of photons by the number of molecules. γ_{tRNA} was calculated in the same pattern, using 1000 nM of tRNA and 10 nM of the dye.

In every experiment, α and proper γ were determined. All the values are collected in **Table S9**.

Table S9. Molecular brightness for YO-PRO-1 dye and formed complexes.

Parameter	Value
α	54
γ_{DNA}	6306
γ_{tRNA}	16224

S12. DNA staining by YO-PRO-1 in living cells

We proved that the equilibrium constant for DNA is larger than tRNA. However, in YO-PRO-1 stained cells, only a small portion of DNA was visible. To address this issue, we performed DAPI counterstaining of the YO-PRO-1 stained cells (**Figure 2F**). DAPI binds primarily to the DNA strands rich in A-T base pairs, thus localizing in chromatin. For the YO-PRO-1, we have identified the three most abundant targets: rRNA, tRNA, and DNA. The confocal images suggest that rRNA and tRNA are the primary binding targets, as the YO-PRO-1 and DAPI staining patterns significantly differ (**Figure S19**A-C). However, when the green-channel images were processed to increase brightness, a weak fluorescence signal of YO-PRO-1-stained chromatin was also visible (**Figure S19**). The brighter spots of YO-PRO-1 stained chromatin colocalize with the brighter spots of DAPI-stained chromatin (yellow and red circles in **Figure S19**B and D). This was also visible in the colocalization plot determined for the whole image (yellow box, **Figure S19**).

This data suggests that YO-PRO-1 can stain DNA in living cells, but the number of accessible targets on tRNA and rRNA makes this binding less visible in confocal imaging.

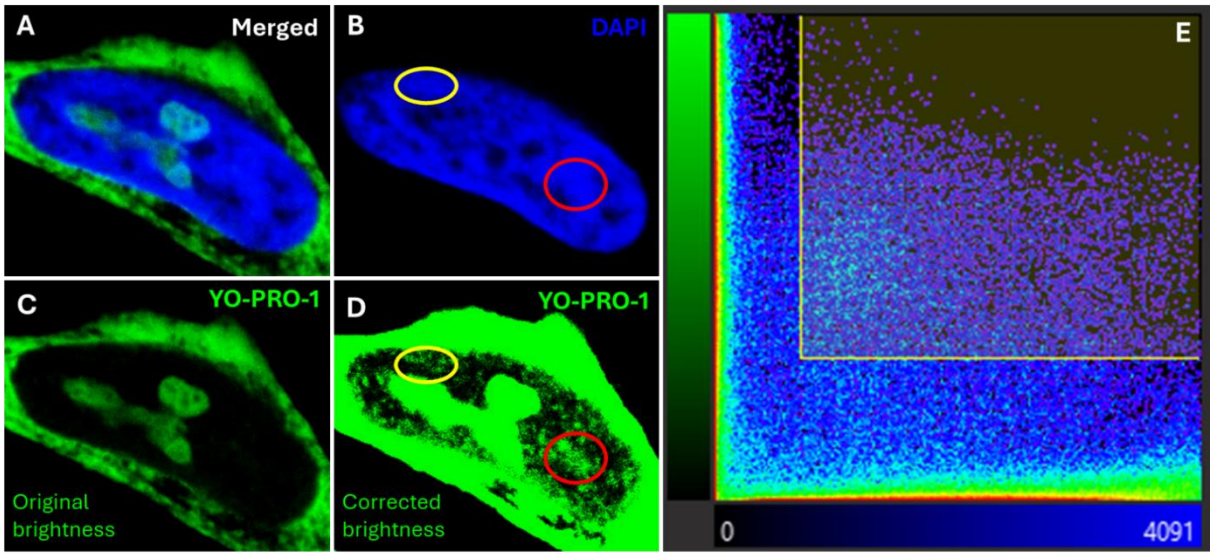

Figure S19. Comparison of DAPI and YO-PRO-1 staining in the nucleus of HeLa cells. Original merged image shows no overlap of the dyes (A). DAPI dye stains whole chromatin (B), while YO-PRO-1 localizes mainly in the nucleoli (C). However image processing of the YO-PRO-1 channel revealed low intensity chromatin staining (D) in the places corresponding with DAPI patterns (compare red and yellow circles in B and D). This co-staining was refelceted by the coloclization pattern analysed with the Imaris software (E).

S13. Cell-cycle dependence of the LSU/tRNA abundance

To address whether free LSU abundance depends on the cell-cycle phase, HeLa cells were synchronized using Aphidicolin[19]. Aphidicolin arrests cells at the G1/S phase border. After aphidicolin removal, cells start their cycle from the S phase and enter the G2 phase ~8 hours later. ~12h after Aphidicolin removal, cell division begins. This synchronization factor was chosen for its reported lack of impact on RNA synthesis.[20]

In our experiment, HeLa cells were seeded on an 8-well plate 48 hours before the experiment. 24 hours later, cells were subjected to a cell culture medium containing Aphidicolin (5 μg/mL) for another 24 hours. After this time, the medium was removed and replaced with the fresh cell culture medium. PBS containing 40 μM YO-PRO-1 was added to each of the wells 30 minutes before the measurements. FCS curves were collected both in the cytoplasm and nucleus of the cell (5 curves/spot). Next, the curves were fitted with the Eq. S11 and fractions of LSU (qLSU) and tRNA (qtRNA) were derived.

It was observed that – especially in the cytoplasm – synchronized cells showed a significantly lower abundance of LSU, suggesting that synchronization itself affects a number of free ribosomal subunits or tRNAs in cells (**Figure S20**). This effect is less pronounced in the nucleus, for which 6h after Aphidicolin removal (late S phase), no significant difference was found as compared to the control (**Figure. S20**, right). In the cytoplasm of synchronized cells, the qLSU/qtRNA ratio gradually decreased, starting from the early S phase up to the end of the G2 phase (**Figure S20**, left). Most probably, it is connected to the increased production of tRNAs, which is known to occur during the S phase.[21] On the other hand, in the nucleus, the qLSU/qtRNA ratio significantly increased only ~6 hours after the S phase started, and after this peak, it returned to the initial value. This interesting behavior can be attributed to an increased supply of ribosomal subunits in preparation for increased protein production demand. Another option – increased export of tRNAs to the cytoplasm was neglected, as this would be accompanied by significantly increased tRNA abundance in the cytoplasm at this time point, which was not observed.

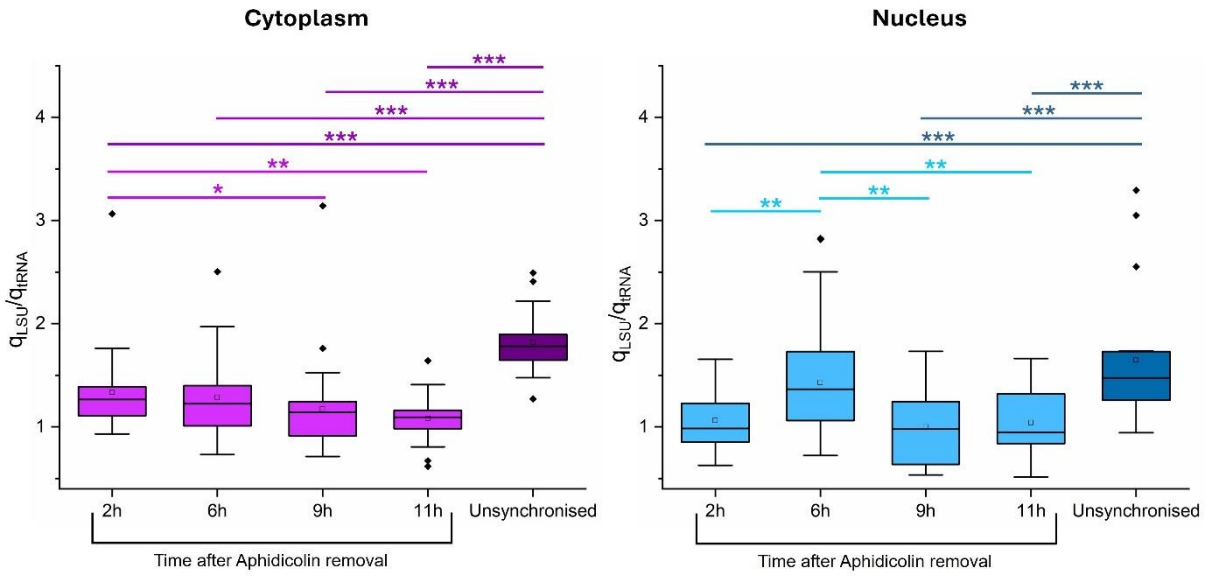

Figure S20. Effect of cell-cycle synchronization on the changes in abundance of LSU and tRNA. Cells were synchronized with the Aphidicolin drug, arresting cells at the G1/S phase border [19]. Results from synchronized cells were compared with unsynchronised control. Statistics were performed using one-way ANOVA, with the following p values marked on graphs: *: $p<0.05$, **: $p<0.005$, ***: $p<0.0005$.

References

[1] Larsson, A.; Carlsson, C.; Jonsson, M.; Albinssont, B. Characterization of the Binding of the Fluorescent Dyes YO and YOYO to DNA by Polarized Light Spectroscopy. *J. Am. Chem. Soc.* **1994**, *116* (19), 8459–8465.

[2] Murade, C. U.; Subramaniam, V.; Otto, C.; Bennink, M. L. Interaction of Oxazole Yellow Dyes with DNA Studied with Hybrid Optical Tweezers and Fluorescence Microscopy. *Biophys. J.* **2009**, *97* (3), 835–843. https://doi.org/10.1016/j.bpj.2009.05.024.

[3] Bubak, G.; Kwapiszewska, K.; Kalwarczyk, T.; Bielec, K.; Andryszewski, T.; Iwan, M.; Bubak, S.; Hołyst, R. Quantifying Nanoscale Viscosity and Structures of Living Cells Nucleus from Mobility Measurements. *J. Phys. Chem. Lett.* **2021**, *12* (1), 294–301. https://doi.org/10.1021/acs.jpclett.0c03052.

[4] Kwapiszewska, K.; Szczepański, K.; Kalwarczyk, T.; Michalska, B.; Patalas-Krawczyk, P.; Szymański, Jędrzej Andryszewski, T.; Iwan, M.; Duszyński, J.; Hołyst, R. Nanoscale Viscosity of Cytoplasm Is Conserved in Human Cell Lines. *J. Phys. Chem. Lett.* **2020**, *11* (16), 6914–6920. https://doi.org/10.1021/acs.jpclett.0c01748.

[5] Kwapiszewska, K.; Kalwarczyk, T.; Michalska, B.; Szczepański, K.; Szymański, J.; Patalas-Krawczyk, P.; Andryszewski, T.; Iwan, M.; Duszyński, J.; Hołyst, R. Determination of Oligomerization State of Drp1 Protein in Living Cells at Nanomolar Concentrations. *Sci. Rep.* **2019**, *9* (1), 1–9. https://doi.org/10.1038/s41598-019-42418-0.

[6] Karpińska, A.; Pilz, M.; Buczkowska, J.; Żuk, P. J.; Kucharska, K.; Magiera, G.; Kwapiszewska, K.; Hołyst, R. Quantitative Analysis of Biochemical Processes in Living Cells at a Single-Molecule Level: A Case of Olaparib-PARP1 (DNA Repair Protein) Interactions. *Analyst* **2021**, *146* (23), 7131–7143. https://doi.org/10.1039/d1an01769a.

[7] Aragón, S. R.; Pecora, R. Fluorescence Correlation Spectroscopy and Brownian Rotational Diffusion. *Biopolymers* **1975**, *14* (1), 119–137. https://doi.org/10.1002/bip.1975.360140110.

[8] Lakowicz, J. R. Fluorescnece Correlation Spectroscopy. In *Principles od Fluorescence Spectroscopy*; Springer Science+Business Media, LLC, 2006; pp 797–840.

[9] Makuch, K.; Hołyst, R.; Kalwarczyk, T.; Garstecki, P.; Brady, J. F. Diffusion and Flow in Complex Liquids. *Soft Matter* **2020**, *16* (1), 114–124. https://doi.org/10.1039/c9sm01119f.

[10] Kalwarczyk, T.; Kwapiszewska, K.; Szczepanski, K.; Sozanski, K.; Szymanski, J.; Michalska, B.; Patalas-Krawczyk, P.; Duszynski, J.; Holyst, R. Apparent Anomalous Diffusion in the Cytoplasm of Human Cells: The Effect of Probes' Polydispersity. *J. Phys. Chem. B* **2017**, *121*

(42), 9831–9837. https://doi.org/10.1021/acs.jpcb.7b07158.

[11] Yoshikawa, H.; Larance, M.; Harney, D. J.; Sundaramoorthy, R.; Ly, T.; Owen-Hughes, T.; Lamond, A. I. Efficient Analysis of Mammalian Polysomes in Cells and Tissues Using Ribo Mega-SEC. *Elife* **2018**, *7*, 1–26. https://doi.org/10.7554/eLife.36530.

[12] Pichon, X.; Bastide, A.; Safieddine, A.; Chouaib, R.; Samacoits, A.; Basyuk, E.; Peter, M.; Mueller, F.; Bertrand, E. Visualization of Single Endogenous Polysomes Reveals the Dynamics of Translation in Live Human Cells. *J. Cell Biol.* **2016**, *214* (6), 769–781. https://doi.org/10.1083/jcb.201605024.

[13] Duncan, R.; Hershey, J. W. Identification and Quantitation of Levels of Protein Synthesis Initiation Factors in Crude HeLa Cell Lysates by Two-Dimensional Polyacrylamide Gel Electrophoresis. *J. Biol. Chem.* **1983**, *258* (11), 7228–7235. https://doi.org/10.1016/s0021-9258(18)32356-1.

[14] Zenklusen, D.; Larson, D. R.; Singer, R. H. Expression in Yeast. **2011**, *15* (12), 1263–1271. https://doi.org/10.1038/nsmb.1514.Single-RNA.

[15] Waldron, C.; Lacroute, F. Effect of Growth Rate on the Amounts of Ribosomal and Transfer Ribonucleic Acids in Yeast. *J. Bacteriol.* **1975**, *122* (3), 855–865. https://doi.org/10.1128/jb.122.3.855-865.1975.

[16] Liang, X.; Zuo, M. Q.; Zhang, Y.; Li, N.; Ma, C.; Dong, M. Q.; Gao, N. Structural Snapshots of Human Pre-60S Ribosomal Particles before and after Nuclear Export. *Nat. Commun.* **2020**, *11* (1), 1–14. https://doi.org/10.1038/s41467-020-17237-x.

[17] García De La Torre, J.; Carrasco, B. Hydrodynamic Properties of Rigid Macromolecules Composed of Ellipsoidal and Cylindrical Subunits. *Biopolymers* **2002**, *63* (3), 163–167. https://doi.org/10.1002/bip.10013.

[18] Kalwarczyk, T.; Tabaka, M.; Holyst, R. Biologistics-Diffusion Coefficients for Complete Proteome of Escherichia Coli. *Bioinformatics* **2012**, *28* (22), 2971–2978. https://doi.org/10.1093/bioinformatics/bts537.

[19] Szczepański, K.; Kwapiszewska, K.; Hołyst, R. Stability of cytoplasmic nanoviscosity during cell cycle of HeLa cells synchronized with Aphidicolin. *Scientific Reports* **2019**, 16486. https://doi.org/10.1038/s41598-019-52758-6.

[20] Pedrali-Noy, G.; Spadari, S.; Miller-Faures, A.; Miller, A. O. A.; Kruppa, J., & Koch, G. Synchronization of HeLa cell cultures by inhibition of DNA polymerase a with Aphidicolin. *Nucleic acids research* **1980**, 8(2), 377-387.

[21] Herrera, M.C.; Chymkowitch, P.; Robertson, J.M.; Eriksson, J.; Bøe, S.O.; Alseth, I.; Enserink, J.M. Cdk1 gates cell cycle-dependent tRNA synthesis by regulating RNA polymerase III activity. *Nucleic Acids Res*. **2018**, 46(22), 11698-11711. doi: 10.1093/nar/gky846.